Supplement of

On the role of trend and variability of hydroxyl radical (OH) in the global methane budget

Yuanhong Zhao, et al.

Correspondence to: Yuanhong Zhao (yuanhong.zhao@lsce.ipsl.fr) and Bo Zheng (bo.zheng@lsce.ipsl.fr)

S1 Estimation of OH production and loss processes

The OH productions including $O(^1D)+H_2O$, $NO+HO_2$, and O_3+HO_2, and OH loss by CO (excluding EMAC) are provided as direct CCMI output listed in the Table S1. OH losses including the reactions with CO (only for EMAC), CH_4, isoprene, and CH_2O, which cannot be directly accessed from CCMI output, are approximately calculated by post-processing the CCMI output of the mixing ratios of reactive species, air pressure, temperature, and reaction coefficients from literature. The reaction coefficients for CESM and EMAC model are from Emmons et al. (2010) and Jöckel et al. (2016), respectively, as listed in table S1. For MRI-ESM1r1 and GEOSCCM, we use the same reaction coefficients with CESM. By comparing the reaction coefficients used in the CESM and EMAC at 273K and 288K, (table S1), one can see those reaction coefficients from different studies show small differences, which are less than 1% for the reaction of CH_4+OH, 2% for isoprene+OH and 6% for CH_2O+OH. The comparisons show that using the same reaction coefficient for different models results in small uncertainties in the estimates of OH loss processes.

Table S1. Estimation of OH production and loss.

By CCMI output	**Production**	**CCMI variable**	**description**
	$O(^1D)+H_2O$	losso1dviah2o	Loss rate of $O(^1D)$ via $O(^1D)$+H2O
	$NO+HO_2$	prodo3viaho2	Production Rate of O_3 via HO_2+NO
	O_3+HO_2	losso3viaho2	Loss Rate of O_3 via O_3+HO_2
	Loss	**CCMI variable**	**description**
	CO+OH	lossco	Rate of CO Oxidation

	Loss	Reaction coefficient[a]	R_{273}[b]	R_{288}[c]
By reaction rates	CO+OH(EMAC)	$1.57\times10^{-13}+3.54\times10^{-33}\times[M]$[d]	2.52×10^{-13}[e]	2.52×10^{-13}
	CH_4+OH(CESM)	$2.45\times10^{-12}\times EXP(-1775.\times1/Ta)$[f]	3.68×10^{-15}	5.16×10^{-15}
	CH_4+OH(EMAC)	$1.85\times10^{-20}Ta^{2.08}\times EXP(-987/Ta)$	3.69×10^{-15}	5.18×10^{-15}
	Isoprene+OH(CESM)	$3.1\times10^{-11}\times EXP(350/Ta)$	1.12×10^{-10}	1.04×10^{-10}
	Isoprene+OH(EMAC)	$2.54\times10^{-11}\times EXP(410/Ta)$	1.14×10^{-12}	1.05×10^{-10}
	CH_2O+OH(CESM)	9×10^{-12}	9×10^{-12}	9×10^{-12}
	CH_2O+OH(EMAC)	$9.52\times10^{-18}\times Ta^{2.03}\times EXP(636/ta)$	8.63×10^{-12}	8.51×10^{-12}

[a] The reaction coefficients are in the unit of cm^{-3} $molec^{-1}$ s^{-1}

[b] R_{273} is the chemical reaction coefficient at 273K

[c] R_{288} is the chemical reaction coefficient at 288K

[d] [M] is the concentration of air molecules in the unit of molec cm^{-3}.

[e] The R273 and R288 for CO+OH are calculated at sea surface pressure (1013.25hPa).

[f] Ta is the air temperature in the unit of K.

S2 Bayesian inversion

Both the two-box model inversions and the 3-D model inversions optimize CH_4 emissions through minimizing the cost function J, which is defined as:

$$J(\boldsymbol{x}) = \frac{1}{2}(\boldsymbol{x}-\boldsymbol{x^b})^T\mathbf{B}^{-1}\left(\boldsymbol{x}-\boldsymbol{x^b}\right) + \frac{1}{2}(H(\boldsymbol{x})-\boldsymbol{y})^T\mathbf{R}^{-1}(H(\boldsymbol{x})-\boldsymbol{y})$$

Here $\boldsymbol{x}$ is the state vector that includes initial conditions and CH_4 emissions. The CH_4 loss (mainly by reaction with OH) is prescribed and not optimized. $\boldsymbol{x^b}$ is the vector of prior emissions, here we use the emission in 2000 from the GCP inventory (Saunois et al., 2019). $H(\boldsymbol{x})$ is the projection from the state vector ($\boldsymbol{x}$) to the observational vector $\boldsymbol{y}$, which is either the two-box model or the 3-D LMDz model.

We set up the two-box model inversions following Turner et al. (2017). The inversions optimize hemispheric yearly emissions and initial conditions of CH_4 through assimilating mean CH_4 mixing ratios in each hemisphere generated from the Earth System Research Laboratory of the US National Oceanic and Atmospheric Administration (NOAA/ESRL, Dlugokencky et al. (1994)). The two box-model can be approximated to a linear system since we do not optimize OH. We assume Gaussian errors and directly estimate the analytical solutions:

$$\boldsymbol{x} = \boldsymbol{x_b} + \boldsymbol{B}\boldsymbol{K}^T(\boldsymbol{K}\boldsymbol{S_A}\boldsymbol{K}^T + \boldsymbol{R})^{-1}(\boldsymbol{y} - H(\boldsymbol{x}))$$

Here K is the linear expression of $H(\boldsymbol{x})$.

The LMDz inversions optimize CH_4 emissions every 8 hours at the model resolution (3.75 °longtitude ×1.85 °latitude) and initial conditions at 20 °×15 °. The observational vector is also constructed by gathering surface observations from the NOAA/ESRL network and assimilated by comparing with model-simulated CH_4 at corresponding model grid-cell and time duration of the observations. The inversion system accesses the CH_4 emissions by iteratively minimizing the cost function J with the M1QN3 algorithm (Gilbert and Lemaréchal, 1989).

S3 MEI

We use the bi-monthly Multivariate ENSO Index (MEI, Wolter et al., 1998; 2001; Kobayashi et al., 2015; Zhang et al., 2019) to represent the ENSO strength. The MEI is estimated as the first principal component of the Empirical Orthogonal Function of the anomalies of 5 ENSO related variables over the tropical Pacific (30 °S-30 °N and 100 °E-70 °W). A positive MEI is corresponding to the El Niño event, while a negative MEI is corresponding to the La Niña event.

Table S2. Global and regional CH_4 losses by reaction with OH and CH_4 emissions estimated by variational inversions (Inv_OH_std and Inv_OH_cli) for the four periods.

CH_4 loss by OH (Tg yr^{-1})	1995-1996		1997-1998		97-98 minus 95-96	
	Inv_OH_std	Inv_OH_cli	Inv_OH_std	Inv_OH_cli	Inv_OH_std	Inv_OH_cli
90 °S-30 °S	44.9	44.4	44.5	44.5	-0.5	0.1
30 °S-30 °N	352.7	348.3	345.3	349.8	-7.4	1.5
30 °-60 °N	69.9	69.1	68.5	69.4	-1.4	0.2
60 °-90 °N	7.8	7.7	7.6	7.7	-0.2	0.0
Global	475.3	469.5	465.9	471.4	-9.4	1.9

CH_4 loss by OH ($Tg\ yr^{-1}$)	2001-2003		2007-2009		07-09 minus 01-03	
	Inv_OH_std	Inv_OH_cli	Inv_OH_std	Inv_OH_cli	Inv_OH_std	Inv_OH_cli
90 °S-30 °S	45.3	44.9	46.1	45.3	0.7	0.3
30 °S-30 °N	355.7	353.0	365.6	356.1	9.9	3.1
30 °-60 °N	71.3	70.0	73.4	70.7	2.1	0.8
60 °-90 °N	7.7	7.8	8.0	7.8	0.3	0.1
Global	480.0	475.7	493.1	480.0	13.0	4.3
CH_4 emissions ($Tg\ yr^{-1}$)	1995-1996		1997-1998		97-98 minus 95-96	
	Inv_OH_std	Inv_OH_cli	Inv_OH_std	Inv_OH_cli	Inv_OH_std	Inv_OH_cli
90 °S-30 °S	15.9	15.8	15.9	16.0	0.0	0.2
30 °S-30 °N	275.0	270.6	277.7	280.1	2.7	9.5
30 °-60 °N	171.9	171.8	176.7	178.6	4.8	6.8
60 °-90 °N	25.3	25.5	26.0	26.3	0.8	0.8
Global	488.1	483.7	496.3	501.0	8.2	17.3
CH_4 emissions ($Tg\ yr^{-1}$)	2001-2003		2007-2009		07-09 minus 01-03	
	Inv_OH_std	Inv_OH_cli	Inv_OH_std	Inv_OH_cli	Inv_OH_std	Inv_OH_cli
90 °S-30 °S	15.0	14.8	14.7	14.1	-0.4	-0.7
30 °S-30 °N	277.1	273.5	292.9	280.8	15.7	7.3
30 °-60 °N	174.4	174.3	186.8	184.6	12.3	10.3
60 °-90 °N	24.1	24.2	26.0	25.7	1.8	1.6
Global	490.8	486.9	520.3	505.2	29.5	18.3

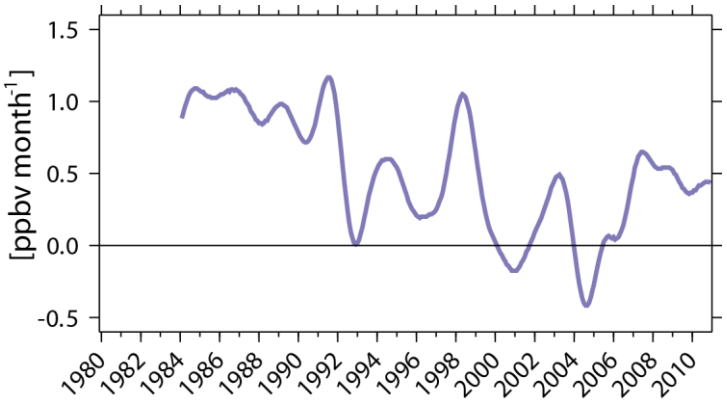

Figure S1. Global CH_4 growth rate computed from NOAA/ESRL observations.

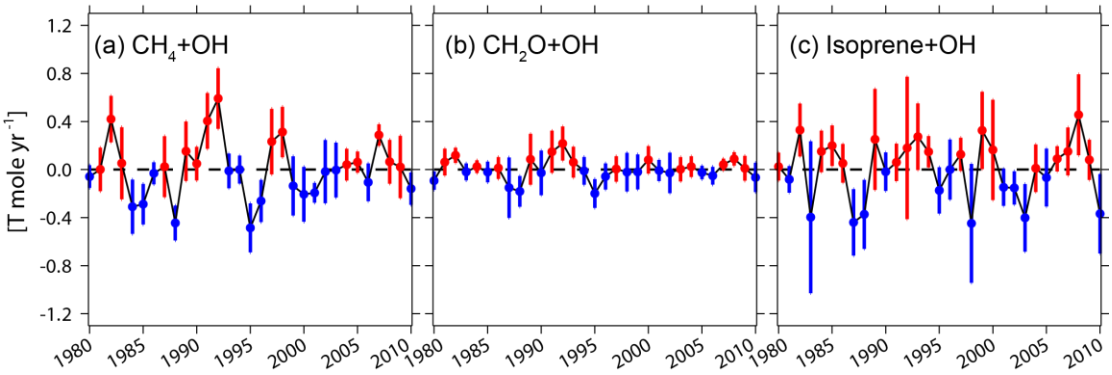

Figure S2. Anomaly of the detrended annual global total OH tendency from the reaction of CH_4+OH, CH_2O+OH, and isoprene+OH. The error bars are the one standard deviation of different models. Red and blue bars indicate positive and negative anomalies of multi-mean values, respectively.

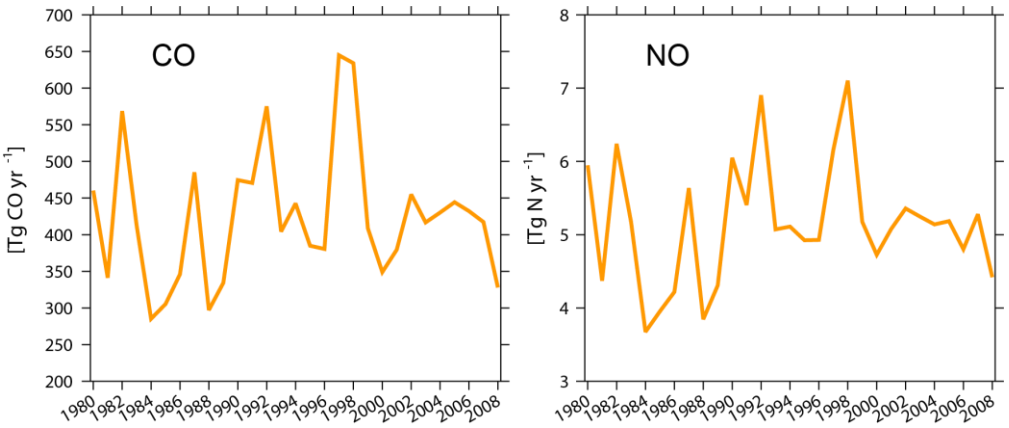

Figure S3. Global total biomass burning emissions for CO (left) and NO (right) from MACCity inventory (Granier et al., 2011) that used in CCMI model simulations.

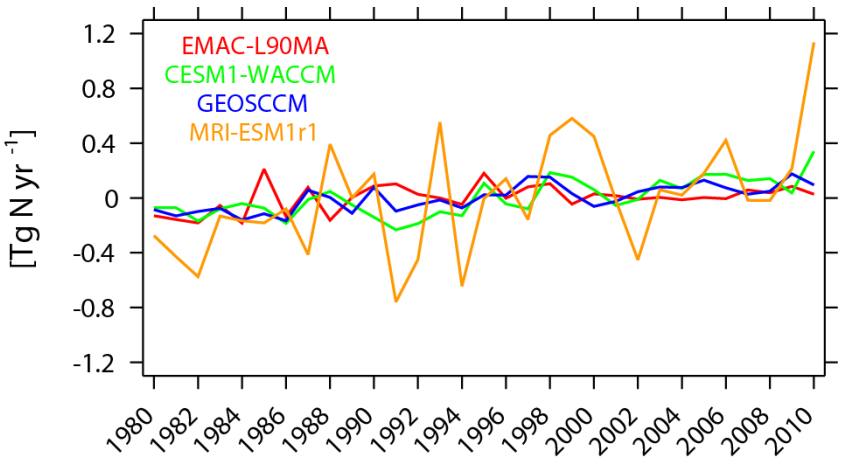

Figure S4. The anomalies in global total lightning emissions of nitrogen oxide (NO, in [Tg N yr^{-1}]) estimated by CCMI models.

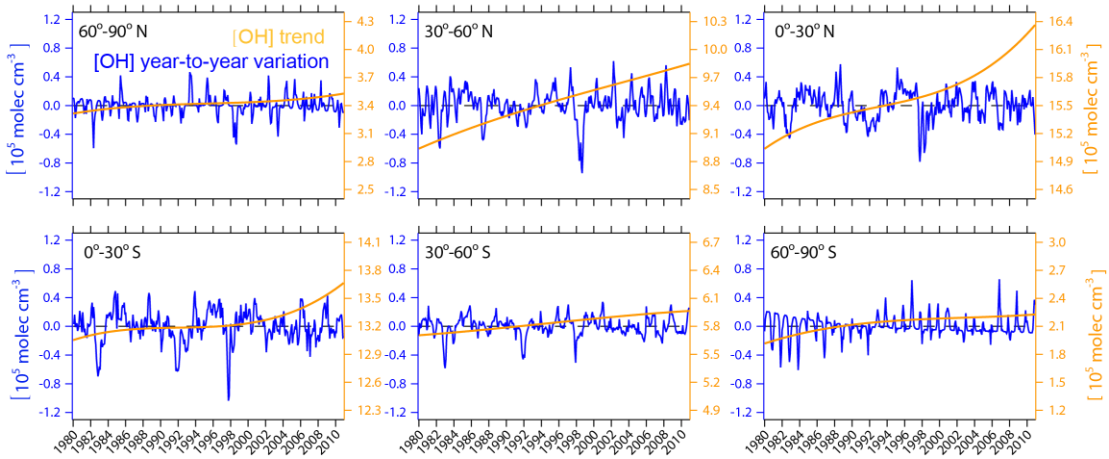

Figure S5. Anomaly of detrended and deseasonalized tropospheric CH_4 reaction weighted monthly mean OH concentration ($[OH]_{CH4}$, CH_4 reaction weighted, blue lines, corresponding to the left axis) and annual mean $[OH]_{CH4}$ with year-to-year variations removed (yellow lines, right axis) averaged over six latitudinal intervals of the multi-model mean OH field.

References

Dlugokencky, NOAA/ESRL ,www.esrl.noaa.gov/gmd/ccgg/trends_ch4/, 2020

Emmons, L. K., Walters, S., Hess, P. G., Lamarque, J. F., Pfister, G. G., Fillmore, D., Granier, C., Guenther, A., Kinnison, D., Laepple, T., Orlando, J., Tie, X., Tyndall, G., Wiedinmyer, C., Baughcum, S. L., and Kloster, S.: Description and evaluation of the Model for Ozone and Related chemical Tracers, version 4 (MOZART-4), Geosci. Model Dev., 3, 43-67, 10.5194/gmd-3-43-2010, 2010.

Granier, C., Bessagnet, B., Bond, T., D'Angiola, A., Denier van der Gon, H., Frost, G. J., Heil, A., Kaiser, J. W., Kinne, S., Klimont, Z., Kloster, S., Lamarque, J.-F., Liousse,

C., Masui, T., Meleux, F., Mieville, A., Ohara, T., Raut, J.-C., Riahi, K., Schultz, M. G., Smith, S. J., Thompson, A., van Aardenne, J., van der Werf, G. R., and van Vuuren, D. P.: Evolution of anthropogenic and biomass burning emissions of air pollutants at global and regional scales during the 1980–2010 period, Climatic Change, 109, 163, https://doi.org/10.1007/s10584-011-0154-1, 2011.

Gilbert, J. C., and Lemaréchal, C.: Some numerical experiments with variable-storage quasi-Newton algorithms, Mathematical programming, 45, 407-435, 1989.

Jöckel, P., Tost, H., Pozzer, A., Kunze, M., Kirner, O., Brenninkmeijer, C. A. M., Brinkop, S., Cai, D. S., Dyroff, C., Eckstein, J., Frank, F., Garny, H., Gottschaldt, K.-D., Graf, P., Grewe, V., Kerkweg, A., Kern, B., Matthes, S., Mertens, M., Meul, S., Neumaier, M., Nützel, M., Oberländer-Hayn, S., Ruhnke, R., Runde, T., Sander, R., Scharffe, D., and Zahn, A.: Earth System Chemistry integrated Modelling (ESCiMo) with the Modular Earth Submodel System (MESSy) version 2.51, Geoscientific Model Development, 9, 1153-1200, 10.5194/gmd-9-1153-2016, 2016.

Kobayashi, S., Ota, Y., Harada, Y., Ebita, A., Moriya, M., Onoda, H., Onogi, K., Kamahori, H., Kobayashi, C., Endo, H., Miyaoka, K., and Takahashi, K.: The JRA-55 Reanalysis: General Specifications and Basic Characteristics, Journal of the Meteorological Society of Japan. Ser. II, 93, 5-48, 10.2151/jmsj.2015-001, 2015.

Saunois, M., Stavert, A. R., Poulter, B., Bousquet, P., Canadell, J. G., Jackson, R. B., Raymond, P. A., Dlugokencky, E. J., Houweling, S., Patra, P. K., Ciais, P., Arora, V. K., Bastviken, D., Bergamaschi, P., Blake, D. R., Brailsford, G., Bruhwiler, L., Carlson, K. M., Carrol, M., Castaldi, S., Chandra, N., Crevoisier, C., Crill, P. M., Covey, K., Curry, C. L., Etiope, G., Frankenberg, C., Gedney, N., Hegglin, M. I., Höglund-Isakson, L., Hugelius, G., Ishizawa, M., Ito, A., Janssens-Maenhout, G., Jensen, K. M., Joos, F., Kleinen, T., Krummel, P. B., Langenfelds, R. L., Laruelle, G. G., Liu, L., Machida, T., Maksyutov, S., McDonald, K. C., McNorton, J., Miller, P. A., Melton, J. R., Morino, I., Müller, J., Murgia-Flores, F., Naik, V., Niwa, Y., Noce, S., O'Doherty, S., Parker, R. J., Peng, C., Peng, S., Peters, G. P., Prigent, C., Prinn, R., Ramonet, M., Regnier, P., Riley, W. J., Rosentreter, J. A., Segers, A., Simpson, I. J., Shi, H., Smith, S. J., Steele, L. P., Thornton, B. F., Tian, H., Tohjima, Y., Tubiello, F. N., Tsuruta, A., Viovy, N., Voulgarakis, A., Weber, T. S., van Weele, M., van der Werf, G. R., Weiss, R. F., Worthy, D., Wunch, D., Yin, Y., Yoshida, Y., Zhang, W., Zhang, Z., Zhao, Y., Zheng, B., Zhu, Q., Zhu, Q., and Zhuang, Q.: The Global Methane Budget 2000-2017, Earth Syst. Sci. Data Discuss., 2019, 1-136, 10.5194/essd-2019-128, 2019.

Wolter, K., and Timlin, M. S.: Measuring the strength of ENSO events: How does 1997/98 rank?, Weather, 53, 315-324, 10.1002/j.1477-8696.1998.tb06408.x, 1998.

Wolter, K., and Timlin, M. S.: El Niño/Southern Oscillation behaviour since 1871 as diagnosed in an extended multivariate ENSO index (MEI.ext), International Journal of Climatology, 31, 1074-1087, 10.1002/joc.2336, 2011.

Zhang, T., Hoell, A., Perlwitz, J., Eischeid, J., Murray, D., Hoerling, M., and Hamill, T. M.: Towards Probabilistic Multivariate ENSO Monitoring, Geophysical Research Letters, 46, 10532-10540, 10.1029/2019gl083946, 2019.